Controlling the magnetotransport properties of magnetic topological insulator $Cr_x(Bi_ySb_{1-y})_{2-x}Te_3$ thin films via molecular beam epitaxy

Jan Karthein,[1,2,*] Jonas Buchhorn,[1,2] Kaycee Underwood,[1,2,†] Abdur Rehman Jalil,[1,3] Max Vaßen-Carl,[1,2] Peter Schüffelgen,[1,2] Detlev Grützmacher,[1,2] and Thomas Schäpers[1,2,‡]

[1]*Peter Grünberg Institut (PGI-9), Forschungszentrum Jülich, 52425 Jülich, Germany*

[2]*JARA-Fundamentals of Future Information Technology, Jülich-Aachen Research Alliance, Forschungszentrum Jülich and RWTH Aachen University, Germany*

[3]*Institute of Experimental Physics III, University of Würzburg, 97070 Würzburg, Germany*

(Received 17 July 2025; revised 23 September 2025; accepted 17 November 2025; published 10 December 2025)

In this work we present a systematic in-depth study of how we can alter the magnetotransport properties of magnetic topological insulator thin films by tuning the parameters of the molecular-beam epitaxy. First, we show how a varying substrate temperature changes the surface morphology and, when chosen properly, leads to a high crystal quality. Next, the effect of the chromium concentration on the film roughness and crystal quality is investigated. Finally, both the substrate temperature and the chromium concentration are investigated with respect to their effect on the magnetotransport properties of the magnetic topological insulator thin films. It becomes apparent that the substrate temperature and the chromium concentration can be used to tune the Fermi level of the film which allows to make the material intrinsically charge neutral. A very low chromium concentration furthermore allows to tune the magnetic topological insulator into a regime where strong superconducting correlations can be expected when combining the material with a superconductor.

DOI: 10.1103/8m2h-83zm

I. INTRODUCTION

Recently, magnetic topological insulators (MTIs) have been proposed as a promising material for the realization of scalable topological quantum computation based on braiding of Majorana fermions [1,2]. MTIs are formed by incorporating magnetic adatoms, such as chromium or vanadium, into a topological insulator lattice [3,4]. Compared to regular topological insulators, the magnetization gives rise to topologically protected edge states [5] that make the use of external magnetic fields for qubit applications obsolete [6]. As a hallmark of the presence of edge-channel transport, the quantum anomalous Hall effect (QAHE) has been measured, which is characterized by a quantized Hall signal and a vanishing longitudinal resistance [7–9]. To enter the field of topological quantum computing, the MTI needs to be proximitized by a superconducting electrode to achieve topological superconductivity. Although induced superconducting correlations in MTIs have already been shown [10], and even an onset of a supercurrent has been measured in an MTI based Josephson junction [11], inducing a hard superconducting gap into this material class remains a challenge. It should be emphasized that in order to realize Majorana fermions and topological superconductivity, the MTI does not necessarily have to be in the quantum anomalous Hall regime [12]. In fact, by performing tight-binding simulations, it was found that a smaller magnetization of the film should result in a larger induced superconducting gap and thus be beneficial for proximitized MTI structures [13,14]. Here we present a systematic in-depth study of the interplay between molecular-beam epitaxy (MBE) growth and magnetotransport of MTI thin films. The MTI material investigated in this work is $Cr_x(Bi_y\ Sb_{1-y})_{2-x}Te_3$ and in the frame of this paper multiple sets of thin films were grown. The study focuses mainly on the effect of the growth temperature T_{sub} and the Cr concentration on the crystal quality and the magnetotransport properties of the MTI thin films. We will first explain the growth dynamics and discuss how the material properties change for these different MBE parameters. Then, the effect of substrate temperature on the magnetotransport properties is investigated. Finally, the effect of varying chromium concentration is studied in transport measurements and the results are discussed. Further information on the structural characterization of the films and the methods used for the electrical characterization can be found in the Supplemental Material [15].

II. GROWTH OPTIMIZATION

To fabricate $Cr_x(Bi_y\ Sb_{1-y})_{2-x}Te_3$ thin films, the precise stoichiometric composition of the base alloy $(Bi_y\ Sb_{1-y})_2Te_3$ which positions the Fermi level inside the bulk gap is crucial. Previous findings [16–18] indicate the optimum stoichiometry to be $Bi_{0.34}Sb_{1.66}Te_3$, having the Bi content at 17%. The

*Contact author: j.karthein@fz-juelich.de

†Present address: Donostia International Physics Center (DIPC), 20018 Donostia-San Sebastián, Spain.

‡Contact author: th.schaepers@fz-juelich.de

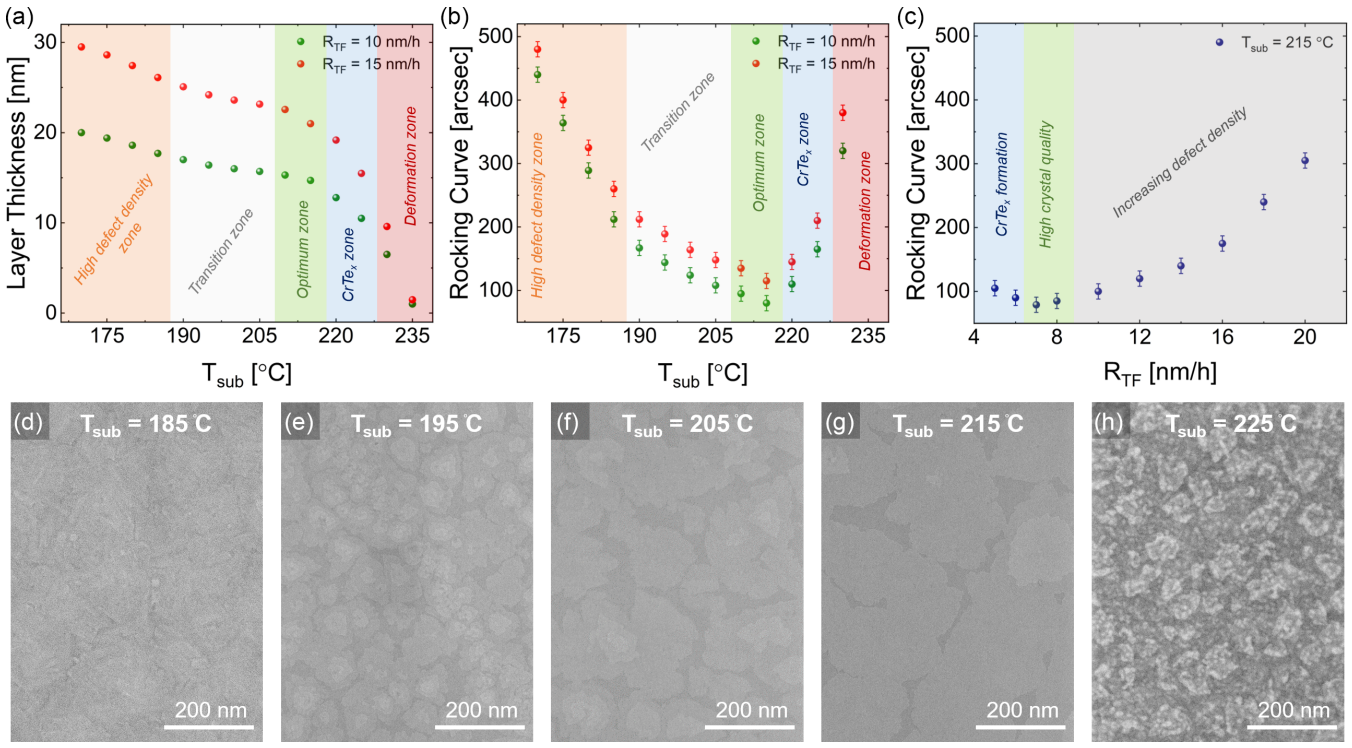

FIG. 1. Identification of optimal parameters for the growth of the $Cr_x(Bi_y\ Sb_{1-y})_{2-x}Te_3$ thin films via MBE. (a) Search for optimal growth temperature T_{sub} where the layer thicknesses are measured via XRR and (b) the crystal quality is assessed by the FWHM value of the rocking curve via XRD measurements. (c) The rocking curve FWHM values as a function of growth rate with epilayers prepared at optimal T_{sub}. The green area always denotes the optimum zone of the growth parameters. (d)–(h) Scanning electron microscopy (SEM) images of $Cr_x(Bi_y\ Sb_{1-y})_{2-x}Te_3$ thin films for increasing substrate temperature. In the aforementioned optimum zone the films are visibly the smoothest.

incorporation of Cr into $(Bi_y\ Sb_{1-y})_2Te_3$ films results in Cr atoms occupying the lattice sites of Bi and Sb. Moreover, Cr, akin to Sb, promotes *p*-type doping in the crystal which requires an increase in Bi content to offset the doping and sustain the Fermi level inside the band gap. The ideal stoichiometry for a quantum anomalous Hall insulator (QAHI), as indicated by Chong *et al.*[19] is $Bi_{0.8}Sb_{1.2}Te_3$, which elevates the Bi content to 40%. Thus, in the preliminary stage of this work, all individual beam fluxes are set to achieve the target stoichiometry of $Cr_{0.2}(Bi_{0.4}Sb_{0.6})_{1.8}Te_3$.

A. Ideal substrate temperature

To determine the ideal growth temperature, the method proposed by Jalil *et al.*[18,20] is employed, for which epilayers with thin-film growth rates R_{TF} of 10 nm/h and 15 nm/h are deposited over a temperature range between 170 °C to 240 °C. Based on the analysis, utilizing x-ray reflectometry (XRR) for thickness measurement and x-ray diffraction (XRD) rocking curve for assessing crystal quality, the entire T_{sub} range is categorized into several zones, as illustrated in Fig. 1(a).

As the name indicates in the high defect-density zone, the relatively low T_{sub} leads to the creation of high density of grains and numerous structural defects, such as domains, rotational twins, and translational-shear faults, which in turn results in elevated values of the full width at half maximum (FWHM) of the rocking curves. In the transition zone, the rising T_{sub} contributes to enhanced crystal quality, resulting in larger grain sizes and subsequently lower FWHM values. The optimum zone yields exceptional crystal quality, featuring the largest grain sizes among all epilayers and significantly fewer structural defects, resulting in the FWHM values below 100 arcseconds. A further increase in T_{sub}, unlike the growth of $(Bi_y\ Sb_{1-y})_2Te_3$ alloy [18], does not lead to an instant deformation zone. Instead, the existence of an intermediate zone is observed. As the substrate temperature T_{sub} increases beyond the optimal range, the adsorption-to-desorption ratio of Sb and Bi atoms decreases, which would typically lead to epilayer deformation. However, rather than inducing such a deformation, the strong adsorption of Cr promotes the segregation of Cr atoms from the $Cr_x(Bi_y\ Sb_{1-y})_{2-x}Te_3$ quintuple-layer structure. This segregation results in the formation of $CrTe_x$ alloy that leaves behind residual and structurally compromised $(Bi_y\ Sb_{1-y})_2Te_3$ layers. $CrTe_x$ is known to be an antiferromagnetic material [21,22] and its presence can adversely affect the desired topological properties. Therefore, its formation should be carefully avoided. Further increases in T_{sub} push the system into the deformation zone, where the adsorption-to-desorption ratio drops sharply, eventually leading to the complete evaporation of the layers. The influence of growth temperature on the surface morphology of the films is also evident in the scanning electron microscopy (SEM) images shown in Figs. 1(d)–1(j).

B. Optimal growth rate

The findings of the previous section conclude that the optimal T_{sub} is 215 °C. While keeping T_{sub} constant at 215 °C,

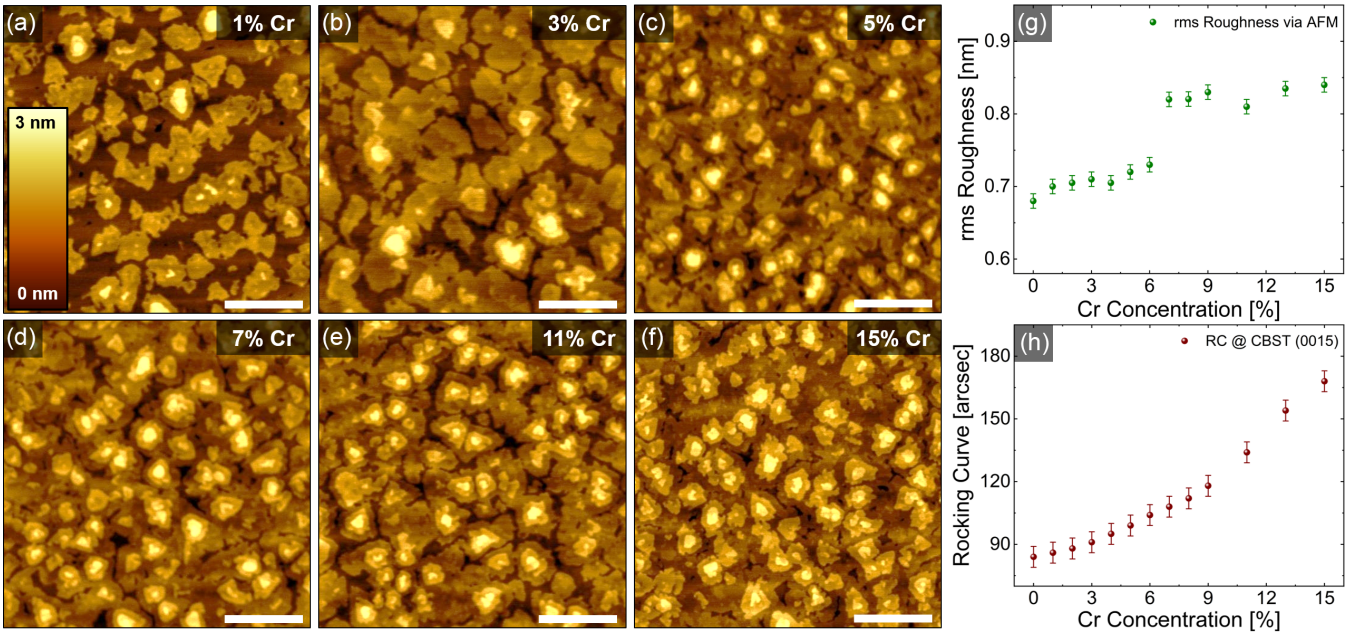

FIG. 2. The effect of increasing chromium concentration on the surface morphology and crystal structure. (a)–(f) AFM images of $Cr_x(Bi_y\ Sb_{1-y})_{2-x}Te_3$ thin films with an increasing x from 1% to 15%. The scale bar is 2 μm. (g) rms surface roughness of the thin films as a function of Cr concentration and (h) the FWHM values of the rocking curve, acquired at the $Cr_x(Bi_y\ Sb_{1-y})_{2-x}Te_3$ (0015) peak in epilayers with increasing Cr contents.

the search for the optimal growth rate is initiated with epilayers being prepared at various R_{TF} ranging from 5 nm/h to 20 nm/h. Systematically decreasing R_{TF} from 20 nm/h to 7 nm/h leads to continuous improvement in the crystal quality. However, once R_{TF} falls below 7 nm/h, the low adsorption-to-desorption ratio of Sb and Bi, combined with the relatively strong adsorption of Cr, results in the formation of $CrTe_x$, similar to as observed in epilayers prepared at higher than optimal T_{sub} [see Fig. 1(c)]. To prevent this and taking into account the stability of the individual beam fluxes to reach the goal of ultralow Cr compositions in this study, an R_{TF} of 8 nm/h is selected for all subsequent growths. The corresponding elemental beam fluxes are as follows: Bi $= 1.6 \times 10^{-8}$ mbar, Sb $= 2.2 \times 10^{-8}$ mbar, and Te $= 7.6 \times 10^{-7}$ mbar, keeping the (Bi + Sb):Te ratio at 1:20 to reduce point defects. The Cr beam flux is insufficient for precise measurement and therefore the temperature of the Cr effusion cell T_{Cr} is utilized to identify any variations in Cr concentrations.

C. Chromium concentration

To obtain consistent thin films with Cr compositions ranging from ultralow (<1%) to relatively high (15%), the temperature of the chromium-effusion cell T_{Cr} is systematically adjusted while keeping the Bi:Sb flux ratio unaltered. Setting T_{Cr} at 930 °C results in no Cr incorporation into the epilayer, as the effective Cr flux is nearly absent. The elemental compositions are measured using Rutherford backscattering spectroscopy (RBS), as outlined in previous research [16]. Starting at $T_{Cr} = 945$ °C, a systematic integration of Cr into the epilayer is observed, with $T_{Cr} = 950$ °C resulting in 1% and $T_{Cr} = 1030$ °C yielding approximately 15% Cr contents in the epilayer.

Multiple epilayers containing various Cr concentrations and thicknesses are prepared and systematically investigated to detect any changes in texture, surface roughness, and crystal quality. Observations indicate that in the absence of Cr, the epilayers consistently initiated nucleation at the substrate step edges, resulting in the development of relatively large grains along the edge line. This, in turn, promotes the emergence of unique linear texture. The integration of Cr leads to a significant shift in dynamics, as the strong adsorption of Cr creates additional nucleation sites. This not only alters the film texture but also leads to smaller grains and a relatively diminished crystal quality. The atomic-force microscopy (AFM) images shown in Figs. 2(a)–2(f) reveal a unique change in the surface texture as the Cr concentration increases in the epilayer. Regarding surface roughness, all epilayers exhibit a root-mean-square (rms) surface roughness of less than 0.85 nm. However, a marginal increase was observed in the epilayers with Cr contents beyond 6% [cf. Fig. 2(g)]. The rocking-curve analysis reveals a steady decline in crystal quality as Cr content increases, mostly attributed to the reduction in grain sizes [cf. Fig. 2(h)].

III. MAGNETOTRANSPORT MEASUREMENTS

In order to extract the essential magnetotransport properties of the thin films, the Hall resistance R_{xy} and sheet resistivity $\rho_{xx}^{\square}$ are determined for the complete range of magnetic field B by using the van der Pauw technique [23]. The results are presented in an illustrative manner in Fig. 3 for an MTI film grown at a substrate temperature of 205 °C and a Cr cell temperature of 990 °C, resulting in a Cr concentration of 6.5%. The Hall resistance R_{xy} is depicted in Fig. 3(a). The

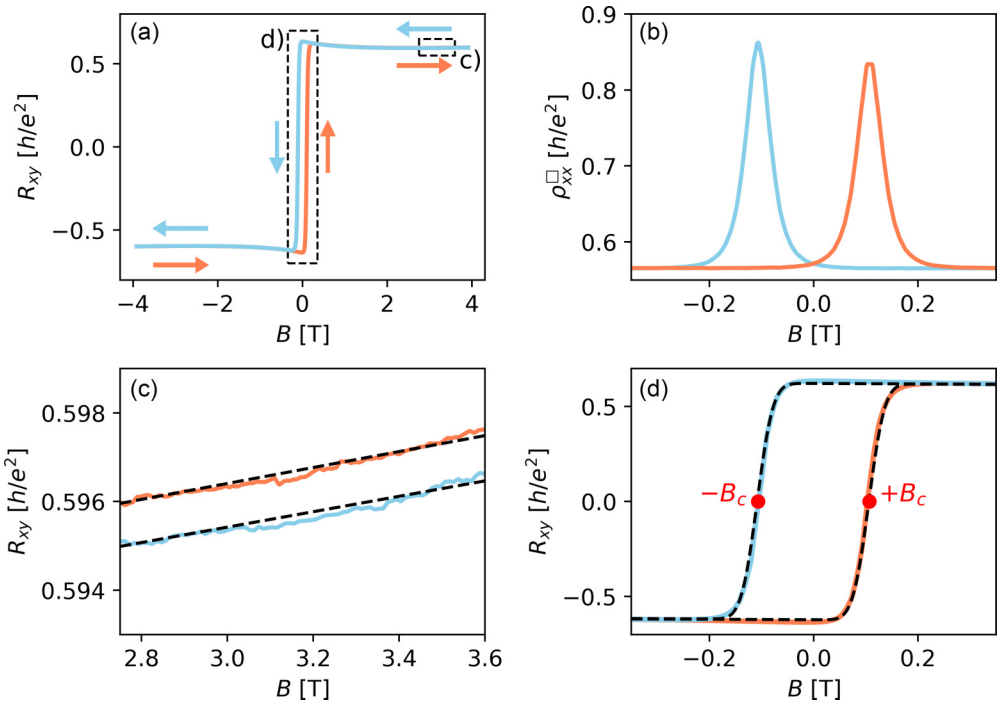

FIG. 3. Resulting curves from the van der Pauw measurements in an exemplary manner for one of the MTI films with a Cr concentration of 6.5%. (a) Hall resistance R_{xy} in units of h/e^2 as a function of magnetic field. The arrows indicate the direction of the magnetic field sweep. The dashed boxes highlight the anomalous part and the regular part of the Hall resistance, respectively. (b) Zoom into the longitudinal resistance ρ_{xx} for small magnetic fields. ρ_{xx} exhibits a peak at the positive and negative coercive field. (c) Zoom into regular part of the Hall resistance. The dashed line is a linear fit from which the two-dimensional charge-carrier density n_{2d} is extracted. (d) Zoom into the anomalous part of the Hall resistance. The dashed line is a sloped error-function fit to the data from which the coercive field B_c and the anomalous Hall resistance R_{AH} can be determined.

sweep direction of the magnetic field is indicated with arrows. It is apparent that the R_{xy} curve consists of a hysteretic part around zero field and shows a linear behavior on B at larger absolute fields. In Fig. 3(b) the sheet resistivity $\rho_{xx}^{\square}$ is shown for a smaller range of magnetic fields. Two peaks are apparent at the field $B = \pm B_c$, with B_c called the coercive field, where R_{xy} in Fig. 3(a) crosses through zero. The two-dimensional charge-carrier density n_{2d} of the material is extracted from R_{xy} via a linear fit (dashed line) to data points at higher magnetic fields where the magnetic hysteresis does not affect the shape of the curve anymore [cf. Fig. 3(c)]. The slight offset of the curves for the different sweep directions of the magnetic field is most likely due to some charging effects. The sheet-carrier density is given by $n_{2d} = 1/(eR_H)$, with R_H being the Hall coefficient which is equal to the slope of the linear fit. The average of n_{2d} for both sweep directions, as well as positive and negative fields, gives the best representation of how many charge carriers are present in the material. The mobility μ can be calculated via $\mu = 1/[en_{2d}\rho_{xx}^{\square}(B = 0)]$. Here, $\rho_{xx}^{\square}(B = 0)$ describes the sheet resistivity at zero magnetic field which can be extracted from the curve shown in Fig. 3(b). The anomalous Hall resistance R_{AH} and the coercive field B_c are extracted from an error-function fit (dashed line) to the hysteretic part of the Hall resistance, as illustrated in Fig. 3(d) [25]. The height of the fitted error function is equal to R_{AH} and the position where the function is zero represents $\pm B_c$, indicated by the red dots.

A. Effect of substrate temperature

As mentioned above, the substrate temperature affects the stoichiometry of the material due to changing surface dynamics during MBE growth assuming that all other parameters remain constant. Hence, even small variations in substrate temperature are also expected to change the magnetotransport properties of the film. The films presented in this section were grown to be within the transition and optimum zone from Fig. 1(a) with a constant Cr cell temperature of $T_{\mathrm{Cr}} = 1015\,^{\circ}\mathrm{C}$.

Figure 4 shows the four major transport parameters, i.e., qn_{2d}, μ, R_{AH}, and B_c, as a function of substrate temperature, extracted from measurements of roughly 20 nm thick films at 4 K. Here, the q prefactor of the charge-carrier density stands for the sign of the Hall slope. This means that for $q = \pm 1$ the dominant charge-carrier types contributing to transport are holes or electrons, respectively. As can be seen in Fig. 4(a), for substrate temperatures up to 210 °C, qn_{2d} is negative, i.e., the transport is electron dominated. Up to 205 °C the carrier concentration is relatively low, i.e., below 1×10^{13} cm^{-2}. At the highest substrate temperature of 215 °C the transport is hole dominated. This means that the Fermi level shifts from the conduction band to the valence band. The mobility as a function of substrate temperature is shown in Fig. 4(b). The highest mobility of about 85 cm^2/Vs is observed for $T_s = 200\,^{\circ}\mathrm{C}$. For the two highest temperatures the mobility is rather low, in the order of 20 cm^2/Vs, most likely due to the presence of charge puddles [26]. As can be seen in

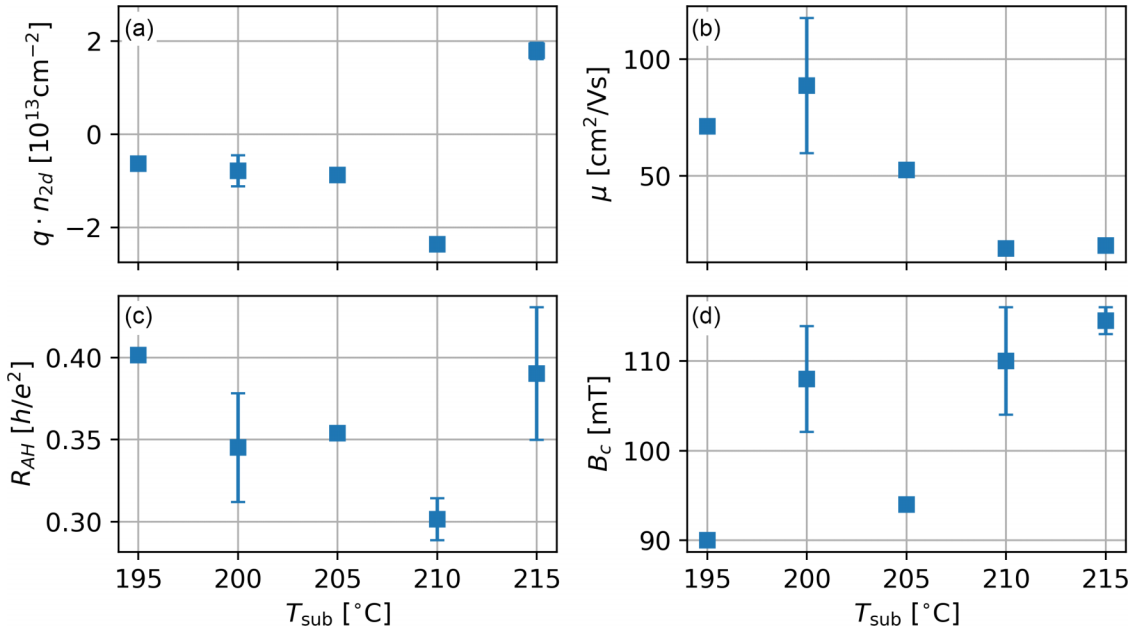

FIG. 4. Magnetotransport parameters of the thin (∼8 nm) $Cr_x(Bi\ Sb)_{2-x}Te_3$ films as a function of substrate temperature extracted from measurements at 4 K. (a) Sheet-carrier concentration n_{2d} multiplied by the sign of the slope of the Hall signal $q = \pm 1$ for hole- and electron-dominated transport, respectively. (b) Mobility μ calculated from n_{2d} and $\rho_{xx}(B = 0)$. (c) Anomalous Hall resistance R_{AH} and (d) coercive field B_c as a function of substrate temperature determined via the error-function fit to R_{xy} at small magnetic fields. Note that in all subplots some data points have error bars while others do not. This is because multiple films were grown for some substrate temperatures, so they were combined into one data point.

Fig. 4(c), at 4 K none of these samples are close to being quantized in Hall resistance, which is apparent from the value of R_{AH} always being smaller than 0.5 h/e^2. Furthermore, the coercive field B_c shown in Fig. 4(d) does not really show a systematic dependence on the substrate temperature. It can be summarized that the shape of the anomalous Hall resistance curve, i.e., the height R_{AH} and the width B_c, is not clearly affected by the substrate temperature. In the next section, a more direct way to change the material composition and hence the magnetic properties is presented by means of changing the Cr concentration of the MTI.

B. Effect of chromium concentration

To systematically vary the Cr concentration in the films, the Cr cell temperature T_{Cr} was varied between 1015 °C and 1022 °C for the more strongly doped, both thicker and thinner films, with $T_{\mathrm{sub}} = 200$ °C resulting in Cr concentrations between 11% and 15%. For the weakly doped thin films T_{Cr} was varied between 950 °C to 1010 °C at $T_{\mathrm{sub}} = 205$ °C resulting in Cr concentrations between 1% and 11.5%. The substrate temperature for the films with varying Cr contents was chosen to be within the previously determined transition zone, as close as possible to the optimum zone, while choosing substrate temperatures that are regarded most promising due to the transport measurements from the previous section. Figure 5 shows once again the four major magnetotransport parameters of the thinner and thicker films with Cr contents from 11.5% to 15%, extracted from measurements at 4 K. The thick films have a thickness of approximately 20 nm and the thin films are roughly 8 nm thick. As can be seen in Fig. 5(a), in the presented range of Cr concentration, qn_{2d} experiences a sign change for both the thick and the thin samples from initially negative, indicating electron-dominated n-type transport, to positive values, indicating mainly hole-dominated p-type transport. For thicker films, the carrier concentration is an order of magnitude larger than for thinner films, since the surface-to-bulk ratio is smaller. Therefore, Fig. 5(b) presents a closer look into the dependence of qn_{2d} on the Cr concentration x for the set of thin films. We find a minimal value of $qn_{2d} = -2.48 \times 10^{13}$ cm^{-2} at $x = 12.5\%$ for the thick films and $qn_{2d} = -8.5 \times 10^{12}$ cm^{-2} at $x = 11.5\%$ for the thin films, respectively. The switch from n-type to p-type transport for an increasing x is expected since Cr is known to be a p-type dopant for the underlying ternary topological insulator $(Bi_xSb_y)_2Te_3$. This means that increasing the Cr concentration allows tuning the Fermi energy to the exchange-gap region of the MTI, which is supported by previous findings [27]. With the Fermi energy located inside the exchange gap, the contribution of the chiral edge state is largest compared to the surface or bulk states.

Normally one would expect the carrier density to become small as qn_{2d} changes sign. However, here it seems more like a divergence before the sign is changed, which is indicated by large error bars for the thick samples with a Cr content of 11.5% in Fig. 5(a). The error bars result from the variation of several different samples grown under the same condition. A large error bar indicates that all samples at this Cr concentration have a Fermi level close to the charge-neutral point (CNP) of the material. The CNP for gapped band structures describes the position of the Fermi energy for which the material is neither n-type nor p-type conductive and hence considered to be charge neutral. Since the potential landscape of the sample

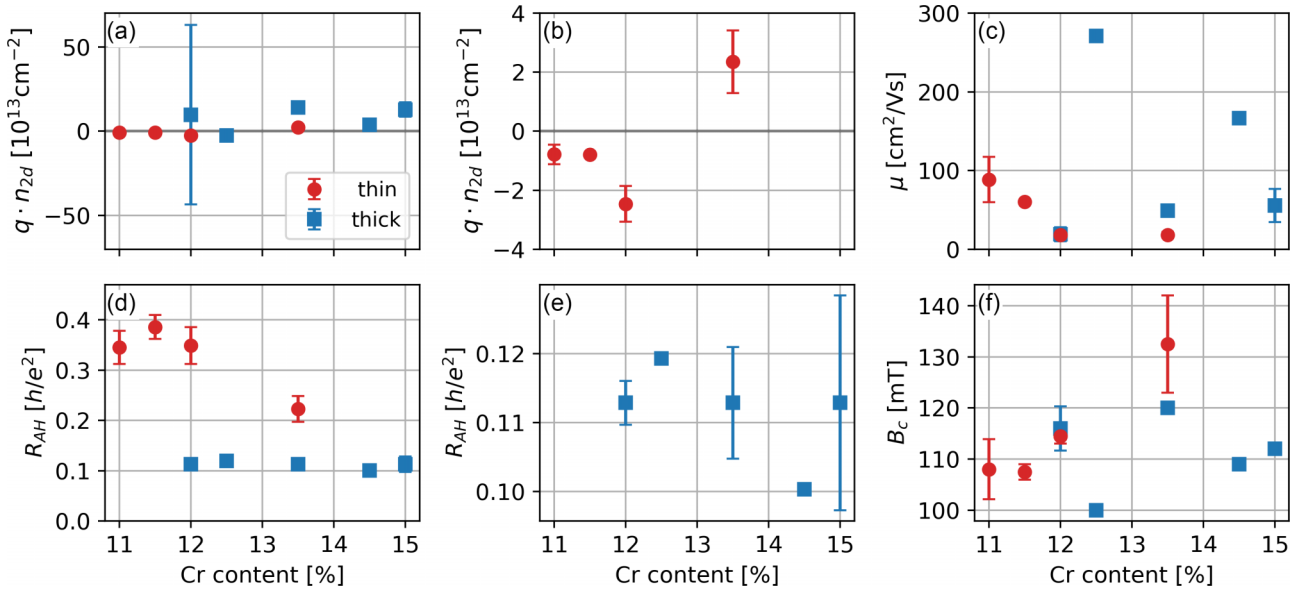

FIG. 5. Transport parameters of thin (∼8 nm) and thick (∼20 nm) $Cr_x(Bi_ySb_{2-y})_{2-x}Te_3$ films measured at 4 K as function of Cr concentration. The values of the thick layers are indicated by blue squares, while the thin samples are represented by red circles. (a) Carrier concentration n_{2d} multiplied by the sign of the slope of the Hall signal $q = \pm 1$ for hole- and electron-dominated transport, respectively. (b) Zoom into a smaller range of n_{2d} to highlight the switch from electron to hole transport for the thin films. (c) Mobility μ for thick and thin samples. (d) Anomalous Hall resistance R_{AH} in h/e^2 as a function of x. The thin samples reach much larger values. (e) Zoom into R_{AH} for the thicker samples. (f) Coercive field B_c.

can fluctuate due to disorder, when the Fermi energy is located close to the CNP it can cut the surface-state conduction and valence band, resulting in p-type and n-type charge puddles [28,29]. Since electrons and holes contribute equally to transport in this regime, a vanishing Hall slope is measured, leading to apparent large-carrier densities. This effect is also noticeable for the thin samples at $12\% > x > 13.5\%$ in Fig. 5(b). For nonmagnetic materials, a two-channel model can be applied, which replaces the classical Hall analysis when two different charge carriers are involved [26,30]. However, due to magnetic hysteresis, such a two-channel model is difficult to apply in our case.

Regarding the mobility μ we find that it is approximately inversely proportional to n_{2d} for both thick and thin samples, as shown in Fig. 5(c). It can be seen that the mobility is generally smaller for the thinner samples compared to the thicker ones which might be due to the larger relative contribution of surface scattering for the thinner layers. The maximum mobility $\mu = 60.7\ \mathrm{cm}^2/\mathrm{Vs}$ for the thin films is found at $x = 11\%$ and the largest mobility for the thick films is given by $\mu = 271\ \mathrm{cm}^2/\mathrm{Vs}$ at $x = 12.5\%$. Another effect of the thickness reduction is seen in R_{AH}, which is presented in Fig. 5(d). Due to the larger surface-to-bulk ratio, the height of the magnetic hysteresis is a factor of up to three larger for the thin samples compared to the thick ones. This results in the thin samples being up to 40% of the quantized value in R_{AH} at 4 K. The thick samples only reach anomalous Hall resistances of around 0.11 h/e^2 with no apparent trend as a function of Cr content as shown in Fig. 5(e). Finally, the coercive field B_c shown in Fig. 5(f) is not much affected by the thickness reduction, although for the thin samples a systematic increase with Cr concentration is observed. This is due to the presence of more ferromagnetic Cr atoms in the film, which leads to a larger exchange gap due to a stronger magnetization [31,32]. Therefore, an indirect indicator of the size of the magnetic-exchange gap that is accessible from transport measurements is the coercive field B_c.

Our findings, as well as previous studies, indicate that one should be able to fine tune the coercive field to a small desired value by fine tuning the Cr concentrations in a smaller regime [27,33]. Therefore, the fourth set of samples with smaller overall Cr concentrations was grown and investigated by transport measurements. Figure 6(a) shows R_{AH} for a range of $1\% > x > 11.5\%$. Although this data set was not optimized

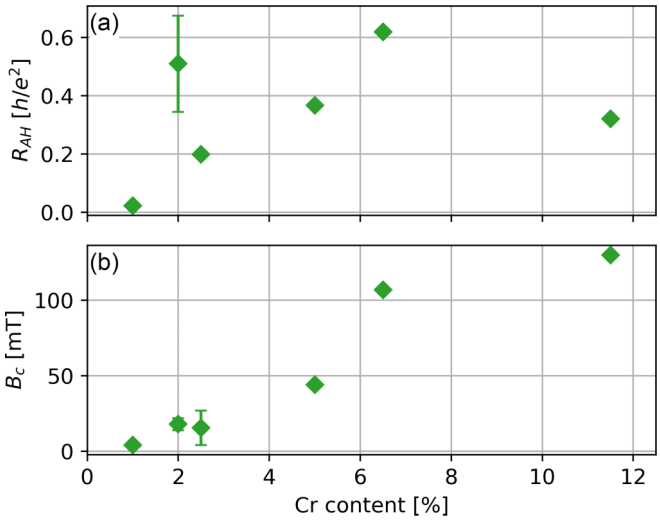

FIG. 6. (a) Anomalous Hall resistance R_{AH} and (b) coercive field B_c determined at a temperature of 1.2 K as a function of the Cr concentration x in a range of 1% to 11.5%.

with respect to charge neutrality, R_{AH} reaches more than 0.6 h/e^2 for two different Cr concentrations. One of the concentrations is 6.5% which is comparable to Cr concentrations in quantized samples [7]. However, the other high value of R_{AH} averaging around 0.5 h/e^2 is found at a very low Cr concentration of only 2%. The coercive field B_c shown in Fig. 6(b) only measures 18 mT at this Cr concentration. It is further apparent that it is indeed possible to fine tune B_c by varying the Cr concentration. At the lowest value of x, the films show almost no magnetic properties anymore. Subsequently, the coercive field increases almost linearly with Cr concentration. A crucial finding is that it is possible to obtain low values of B_c, and thus small magnetic-exchange gaps, in a reproducible fashion. As mentioned before, films with a smaller B_c and hence a smaller magnetization, resulting in a smaller magnetic-exchange gap, are theoretically predicted to be more beneficial for inducing superconductivity into the MTI.

IV. CONCLUSION

Magnetic topological insulators are predicted to have interesting applications in quantum computation. Controlling the parameters of the molecular-beam epitaxy during growth of the MTI thin films allows to reach exceptional crystal quality and low surface roughness in combination with large grain sizes. Furthermore the MBE enables precise control over the material composition which can be used to alter the magnetotransport properties of the thin films. This allows to tune the MTI thin films into a regime where strong-induced superconducting correlations are expected when combining them with conventional superconductors.

ACKNOWLEDGMENTS

We thank Herbert Kertz for technical assistance. This work is supported by the QuantERA grant MAGMA and by the Deutsche Forschungsgemeinschaft (DFG, German Research Foundation) under Grant No. 491798118. In addition, we received funding from DFG under Germany's Excellence Strategy—Cluster of Excellence Matter and Light for Quantum Computing (ML4Q) Grant No. EXC 2004/1 – 390534769 as well as financial support by the Bavarian Ministry of Economic Affairs, Regional Development and Energy within Bavaria's High-Tech Agenda Project "Bausteine für das Quantencomputing auf Basis topologischer Materialien mit experimentellen und theoretischen Ansätzen" (Grant No. 07 02/686 58/1/21 1/22 2/23).

DATA AVAILABILITY

The data that support the findings of this article are openly available [34].

[1] C.-Z. Chen, Y.-M. Xie, J. Liu, P. A. Lee, and K. T. Law, Quasi-one-dimensional quantum anomalous Hall systems as new platforms for scalable topological quantum computation, Phys. Rev. B **97**, 104504 (2018).

[2] X.-L. Qi, T. L. Hughes, and S.-C. Zhang, Chiral topological superconductor from the quantum Hall state, Phys. Rev. B **82**, 184516 (2010).

[3] C.-Z. Chang, J. Zhang, M. Liu, Z. Zhang, X. Feng, K. Li, L.-L. Wang, X. Chen, X. Dai, Z. Fang *et al.*, Thin films of magnetically doped topological insulator with carrier-independent long-range ferromagnetic order, Adv. Mater. **25**, 1065 (2013).

[4] L. Zhang, D. Zhao, Y. Zang, Y. Yuan, G. Jiang, M. Liao, D. Zhang, K. He, X. Ma, and Q. Xue, Ferromagnetism in vanadium-doped Bi_2Se_3 topological insulator films, APL Mater. **5**, 076106 (2017).

[5] R. Yu, W. Zhang, H.-J. Zhang, S.-C. Zhang, X. Dai, and Z. Fang, Quantized anomalous Hall effect in magnetic topological insulators, Science **329**, 61 (2010).

[6] Y. Tokura, K. Yasuda, and A. Tsukazaki, Magnetic topological insulators, Nat. Rev. Phys. **1**, 126 (2019).

[7] C.-Z. Chang, J. Zhang, X. Feng, J. Shen, Z. Zhang, M. Guo, K. Li, Y. Ou, P. Wei, L.-L. Wang *et al.*, Experimental observation of the quantum anomalous Hall effect in a magnetic topological insulator, Science **340**, 167 (2013).

[8] C.-Z. Chang, W. Zhao, D. Y. Kim, H. Zhang, B. A. Assaf, D. Heiman, S.-C. Zhang, C. Liu, M. H. Chan, and J. S. Moodera, High-precision realization of robust quantum anomalous Hall state in a hard ferromagnetic topological insulator, Nat. Mater. **14**, 473 (2015).

[9] M. Mogi, R. Yoshimi, A. Tsukazaki, K. Yasuda, Y. Kozuka, K. Takahashi, M. Kawasaki, and Y. Tokura, Magnetic modulation doping in topological insulators toward higher-temperature quantum anomalous Hall effect, Appl. Phys. Lett. **107**, 182401 (2015).

[10] A. Uday, G. Lippertz, K. Moors, H. F. Legg, R. Joris, A. Bliesener, L. M. Pereira, A. Taskin, and Y. Ando, Induced superconducting correlations in a quantum anomalous Hall insulator, Nat. Phys. **20**, 1589 (2024).

[11] T. Jansen, E. Kochetkova, A. Isaeva, A. Brinkman, and C. Li, Josephson coupling across magnetic topological insulator $MnBi_2Te_4$, Commun. Mater. **5**, 214 (2024).

[12] J. Legendre, E. Zsurka, D. Di Miceli, L. Serra, K. Moors, and T. L. Schmidt, Topological properties of finite-size heterostructures of magnetic topological insulators and superconductors, Phys. Rev. B **110**, 075426 (2024).

[13] D. Burke, D. Heffels, K. Moors, P. Schüffelgen, D. Grützmacher, and M. R. Connolly, Robust Majorana bound states in magnetic topological insulator nanoribbons with fragile chiral edge channels, Phys. Rev. B **109**, 045138 (2024).

[14] E. Zsurka, D. Di Miceli, J. Legendre, L. Serra, D. Grützmacher, T. L. Schmidt, and K. Moors, Optimizing proximitized magnetic topological insulator nanoribbons for Majorana bound states, Phys. Rev. B **112**, 094504 (2025).

[15] See Supplemental Material at http://link.aps.org/supplemental/10.1103/8m2h-83zm for more details on the structural characterization and methods used for the electrical measurements, which includes Refs. [19,20,23,24].

[16] A. R. Jalil, Engineering topological superlattices and their epitaxial integration in selectively grown hybrid nanostructures via MBE, Dissertation Thesis: Ph.D., RWTH Aachen University, Aachen, Germany, 2022.

[17] P. Schüffelgen, D. Rosenbach, C. Li, T. W. Schmitt, M. Schleenvoigt, A. R. Jalil, S. Schmitt, J. Kölzer, M. Wang, B. Bennemann *et al.*, Selective area growth and stencil lithography for *in situ* fabricated quantum devices, Nat. Nanotechnol. **14**, 825 (2019).

[18] A. R. Jalil, P. Schüffelgen, H. Valencia, M. Schleenvoigt, C. Ringkamp, G. Mussler, M. Luysberg, J. Mayer, and D. Grützmacher, Selective area epitaxy of quasi-1-dimensional topological nanostructures and networks, Nanomaterials **13**, 354 (2023).

[19] S. K. Chong, P. Zhang, J. Li, Y. Zhou, J. Wang, H. Zhang, A. V. Davydov, C. Eckberg, P. Deng, L. Tai *et al.*, Electrical manipulation of topological phases in a quantum anomalous Hall insulator, Adv. Mater. **35**, 2207622 (2023).

[20] A. R. Jalil, X. Hou, P. Schüffelgen, J. H. Bae, E. Neumann, G. Mussler, L. Plucinski, and D. Grützmacher, Phase-Selective epitaxy of trigonal and orthorhombic bismuth thin films on Si (111), Nanomaterials **13**, 2143 (2023).

[21] N. Abuawwad, M. d. S. Dias, H. Abusara, and S. Lounis, $CrTe_2$ As a two-dimensional material for topological magnetism in complex heterobilayers, Phys. Rev. B **108**, 094409 (2023).

[22] A. A. Katanin and E. M. Agapov, Magnetic properties of monolayer, multilayer, and bulk $CrTe_2$, Phys. Rev. B **111**, 035118 (2025).

[23] L. J. van der Pauw, A method of measuring the resistivity and hall coefficient on lamellae of arbitrary shape, Philips Tech. Rev. **20**, 220 (1958).

[24] G. Qiu, H.-Y. Yang, S. K. Chong, Y. Cheng, L. Tai, and K. L. Wang, Manipulating topological phases in magnetic topological insulators, Nanomaterials **13**, 2655 (2023).

[25] E. Zimmermann, M. Schleenvoigt, A. Rupp, G. Behner, J. Karthein, J. Teller, P. Schüffelgen, H. Lüth, D. Grützmacher, and T. Schäpers, Fourier transformation based analysis routine for intermixed longitudinal and transversal hysteretic data for the example of a magnetic topological insulator, J. Phys. Mater. **7**, 015015 (2024).

[26] N. Ito, R. Masutomi, and T. Okamoto, Cancellation of electron and hole contributions to the Hall effect in ultrathin Bi films grown on GaAs (110), Phys. Rev. B **105**, 205434 (2022).

[27] X. Kou, M. Lang, Y. Fan, Y. Jiang, T. Nie, J. Zhang, W. Jiang, Y. Wang, Y. Yao, L. He *et al.*, Interplay between different magnetisms in Cr-doped topological insulators, ACS Nano **7**, 9205 (2013).

[28] C. Weyrich, M. Drögeler, J. Kampmeier, M. Eschbach, G. Mussler, T. Merzenich, T. Stoica, I. E. Batov, J. Schubert, L. Plucinski, B. Beschoten, C. M. Schneider, C. Stampfer, D. Grützmacher, and T. Schäpers, Growth, characterization, and transport properties of ternary $(Bi_{1-x}Sb_x)_2$ Te_3 topological insulator layers, J. Phys.: Condens. Matter **28**, 495501 (2016).

[29] G. Lippertz, A. Bliesener, A. Uday, L. M. C. Pereira, A. A. Taskin, and Y. Ando, Current-induced breakdown of the quantum anomalous Hall effect, Phys. Rev. B **106**, 045419 (2022).

[30] N. W. Ashcroft and N. Mermin, *Solid State, Physics* (Rinehart and Winston, New York,1976).

[31] H.-Z. Lu, J. Shi, and S.-Q. Shen, Competition between weak localization and antilocalization in topological surface states, Phys. Rev. Lett. **107**, 076801 (2011).

[32] Y. Chen, J.-H. Chu, J. Analytis, Z. Liu, K. Igarashi, H.-H. Kuo, X. Qi, S.-K. Mo, R. Moore, D. Lu *et al.*, Massive Dirac fermion on the surface of a magnetically doped topological insulator, Science **329**, 659 (2010).

[33] Y. Ou, C. Liu, L. Zhang, Y. Feng, G. Jiang, D. Zhao, Y. Zang, Q. Zhang, L. Gu, Y. Wang *et al.*, Heavily Cr-doped $(Bi,Sb)_2Te_3$ as a ferromagnetic insulator with electrically tunable conductivity, APL Mater. **4**, 086101 (2016).

[34] J. Karthein, J. Buchhorn, K. Underwood, A. R. Jalil, P. Schüffelgen, D. Grützmacher, and T. Schäpers, Data for: Controlling the magnetotransport properties of magnetic topological insulator thin films from $Cr_x(Bi_y$ $Sb_{1-y})_{2-x}Te_3$ via molecular beam epitaxy, JülichDATA (2025), https://data.fz-juelich.de/dataset.xhtml?persistentId=doi:10.26165/JUELICH-DATA/VTVHYF.